PROTEINS
STRUCTURE ■ FUNCTION ■ BIOINFORMATICS

Fibril elongation mechanisms of HET-s prion-forming domain: Topological evidence for growth polarity

Marco Baiesi, Flavio Seno, and Antonio Trovato*

Department of Physics, Padua University, CNISM, Padova Unit, Padova I-35131, Italy

ABSTRACT

The prion-forming C-terminal domain of the fungal prion HET-s forms infectious amyloid fibrils at physiological pH. The conformational switch from the nonprion soluble form to the prion fibrillar form is believed to have a functional role, as HET-s in its prion form participates in a recognition process of different fungal strains. On the basis of the knowledge of the high-resolution structure of the prion forming domain HET-s(218-289) in its fibrillar form, we here present a numerical simulation of the fibril growth process, which emphasizes the role of the topological properties of the fibrillar structure. An accurate thermodynamic analysis of the way an intervening HET-s chain is recruited to the tip of the growing fibril suggests that elongation proceeds through a dock and lock mechanism. First, the chain docks onto the fibril by forming the longest *β*-strands. Then, the re-arrangement in the fibrillar form of all the rest of the molecule takes place. Interestingly, we also predict that one side of the HET-s fibril is more suitable for sustaining its growth with respect to the other. The resulting strong polarity of fibril growth is a consequence of the complex topology of HET-s fibrillar structure, as the central loop of the intervening chain plays a crucially different role in favoring or not the attachment of the C-terminus tail to the fibril, depending on the growth side.

Proteins 2011; 79:3067–3081.

Key words: protein aggregation; dock and lock mechanism; coarse-grained models; Monte Carlo simulations; topology-based models.

INTRODUCTION

Prions are self-propagating, usually amyloid like protein aggregates[1] that are responsible for transmissible diseases. Examples of prion diseases are scrapie in sheep,[2] bovine spongiform encephalopathy[3] in cattle, and new variant Creutzfeldt–Jakob disease[4] in humans. In contrast to these disease-related cases, several proteins displaying prion properties are well known in yeast and fungi.[5] The HET-s prion protein produced by the filamentous fungus *Podospora anserina* is thought to be involved in a specific function. The switching on of its prion form triggers the programmed-cell-death phenomenon named "heterokaryon incompatibility",[6,7] which can prevent different forms of parasitism, by inducing the death of the heterokaryon formed by cell fusion of different fungal strains. The proteinase K-resistant core of the prion fibrils formed by the C-terminal residues 218–289 (PFD: prion-forming domain) is unstructured in solution and forms infectious fibrils *in vitro*.[8] Earlier work showed that HET-s PFD fibrils consist of four β-strands forming two windings of a β-solenoid,[9] without giving further information about the details of the intramolecular and intermolecular β-sheet architecture. Recently, the structure of HET-s PFD has been determined[10] on the basis of NMR-derived intramolecular and intermolecular distance restraints.[11,12] This is the only atomic-resolution structural model of an infectious fibrillar state reported to date. On the basis of 134 intramolecular and intermolecular experimental distance restraints, HET-s PFD forms a left-handed β-solenoid, with each molecule forming two helical windings, a compact hydrophobic core, at least 23 hydrogen bonds, three salt bridges, and two asparagine ladders see Fig. 1(a,b). The model is supported by electronic diffraction and scanning transmission electronic microscopy.[10]

Despite the tremendous economical and social relevance of diseases related to prion infections and protein aggregation and the enormous quantity of research devoted to their study, the mechanisms that rule and trigger fibril formation and elongation remain mostly elusive: the nature of protein aggregation, its limited structural order, its insolubility in water, and its involvement with the cell membrane render its experimental study extremely difficult. For these reasons, relevant breakthroughs to understand the principles of amyloid formation and fibril growth might come from numerical simulations.

Grant sponsor: University of Padua; Grant number: Progetto di Ateneo n. CPDA083702.
*Correspondence to: Antonio Trovato, Department of Physics, Padua University, CNISM, Padova Unit, Via Marzolo 8, Padova I-35131, Italy E-mail: trovato@pd.infn.it
Received 24 March 2011; Revised 23 June 2011; Accepted 7 July 2011
Published online 22 July 2011 in Wiley Online Library (wileyonlinelibrary.com). DOI: 10.1002/prot.23133

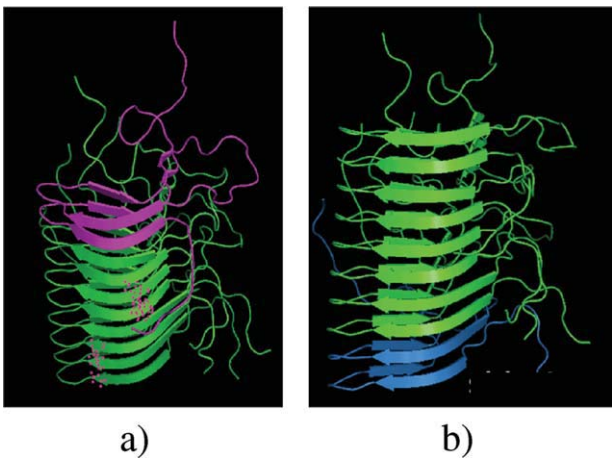

Figure 1

High-resolution experimental structure of HET-s fibril. Side view of the five molecules present in the fibrillar structure of HET-s PFD calculated with NMR restraints (PDB code: 2RNM). In (a), the monomer on the top of the fibril (Chain E) is drawn in violet, whereas in (b), the bottom monomer (Chain A) is drawn in blue. [Color figure can be viewed in the online issue, which is available at wileyonlinelibrary.com.]

Recent advances in hardware and methodology have allowed for realistic atomic-resolution molecular dynamics (MD) simulations with physics-based potentials of small fibrils consisting of a few monomer units that make possible to span time scales of hundreds of nanoseconds[13–19] and even of microseconds for smaller systems.[20–22] These results were mainly obtained by studying the amyloid β(Aβ)-peptide, related to the Alzheimer's disease,[23] or its mutants and fragments. In this context, experimental observations had first originated the proposal that incoming Aβ-monomers associate with the elongating fibril through a two-stage "dock and lock" kinetic mechanism.[24] In the first stage, an unstructured monomer docks onto the fibril while maintaining some degree of conformational freedom. In the second stage, the monomer locks into the final fibril state. Such a mechanism was later confirmed and refined, also in the context of Aβ-peptide oligomerization, by other experimental and simulation studies.[18,25,26] The dock and lock mechanism was further used, for the Aβ-peptide, to describe fibril elongation within a thermodynamic context, in all-atom MD simulations.[27] A continuous docking stage was observed to occur over a wide temperature range without free energy barriers or intermediates, whereas the locking stage at lower temperatures was characterized by many competing free energy minima in a rugged landscape.

For the fibrillar HET-s PFD protein, it was possible with MD atomistic simulation to probe the stability of the NMR structure on a 10-ns timescale and to predict the behavior of the salt bridge network.[28] On the other hand, typical elongation times for amyloid fibrils formed by HET-s PFD are of the order of hours,[29] so that coarse-grained approaches, in which protein chains and amino acid interactions are modeled in a simplified way, are mandatory to investigate such longer time scales. Indeed, despite the difficulty of finding reliable energy functions, these approaches have been successfully used in outlining general aspects of the full phase diagram of a generic aggregating polypeptide system,[30–32] to emphasize the importance of the contribution of hydrophobic interactions and hydrogen bonding in the aggregation process of the Aβ-peptide[33–38] and even to study the mechanisms of monomer addition for the Aβ-peptide and some of its mutants.[39–41]

In this article, to describe the fibril elongation mechanisms of a relatively long protein domain such as HET-s PFD, we prefer to use a still different coarse-grained approach because in this case there is the unique advantage of knowing the fibril structure from experiments. At a general level, our strategy falls in the class of approaches used in protein folding that builds on the importance of the native-state topology in steering the folding process.[42] In its simplest example, the formation of contacts is favored only for pairs of amino acids that are found interacting in the native state, but non-native sequence-dependent interactions could be introduced as well. Despite the simplicity of this scheme, in the past few years, an increasing number of experimental and theoretical studies have confirmed the utility of the Go-like approach in the characterization of various aspects of protein folding and binding processes.[43–50]

The study of protein aggregation has been already tackled by using Go-like models[51,52]; however, because of the absence of experimental information on the fibrillar structure, hypothetical aggregate conformations had to be introduced to build the Go-energy function driving aggregation. Moreover, topology-based models, with reduced effect of nonnative interactions, correspond to funneled energy landscapes and therefore their application should be limited to situations in which proteins are evolutionarily designed to follow the principle of minimal frustration,[53] which results in a faster search through the many possible alternatives. In general, a funneled energy landscape is not expected in nonfunctional fibril formation. Therefore, the accurate knowledge of its structure, the complex intrachain topology, and the plausible involvement in a functional process makes HET-s PFD a suitable and, at the moment, unique candidate to exploit successfully Go-like models to study amyloid formation and fibril elongation mechanisms.

Within this approach, implemented through a Monte Carlo procedure combined with replica exchange methods, we analyze the full thermodynamic properties of the fibril elongation process, that is the association of a free chain to the already formed fibrillar structure of HET-s PFD under different concentrations. The behavior of

both energies and heat capacities shows that the association process becomes more cooperative for concentrations in the range ($\sim$10 μM) of standard *in vitro* experiment.[54] A careful study of the association process shows that fibril elongation is triggered by the docking of the free chain onto the fibril in a concentration-dependent mechanism that involves the formation of both interchain and intrachain hydrogen bonds stabilizing the longest β-strands, rapidly followed by the assembly of the full domain. This behavior is similar to the dock and lock mechanism proposed for the Aβ-fibril formation.[24,27]

Another interesting aspect emerges clearly: elongation proceeds differently according to which side of the fibril [see Fig. 1(a,b)] is used as the growing end. Elongation from one side is clearly favored with respect to the other side, implying a strong polarity in the growth of HET-s PFD fibrils, which may even lead to unidirectional elongation. Polarity in fibril growth is a feature already discussed in the literature for other amyloid-forming proteins, in both experiments[55,56] and numerical simulations.[27,57] Our data suggest that growth polarity can be explained for HET-s PFD on the basis of the complex topological properties of its fibrillar structure. A key role is played by the behavior of one long loop connecting two β-strands in consecutive rungs of the fibrillar structure. Depending on the elongation side, this loop may help or not the winding of the C-terminal part of the attaching chain into the fibrillar form. Because it is known that the prion loses its infectivity on partial deletion of that loop,[9] we argue that this topological mechanism may be important for functional fibril growth.

METHODS

Protein chain representation and energy function

Chains A and B were selected from the NMR structure of HET-s PFD (PDB code: 2rnm), where chain B stays on top of Chain A along the fibril. We keep one chain frozen and the other one is free. In the top elongation mode, Chain B is free and Chain A is frozen, whereas in the bottom elongation mode, Chain A is free and Chain B is frozen. The free chain is allowed to move in a hemisphere of radius L defined by $x^2 + y^2 + z^2 < L^2$, $0 < z < L$ ($-L < z < 0$) for top (bottom) elongation. The frozen chain is placed with center-of-mass (i.e. average C^α) coordinates $x_{cm} = y_{cm} = 0$ (i.e. on the hemisphere axis) and $z_{cm} = +5.60$ Å ($z_{cm} = -2.35$ Å) for top (bottom) elongation, rotated in such a way that the fibril axis is parallel to the hemisphere axis. The center-of-mass position along the hemisphere axis is chosen to expose only one "sticky" end of the frozen chain to the free chain, by placing the other end roughly on the hemisphere base $z = 0$. This allows a smaller computational effort, at the expense of prohibiting conformations that we do not expect to affect in a relevant way the binding of the free chain on the exposed end of the full fibril, here represented by the frozen chain. The portion of HET chain that we simulate goes from position 217 to position 289, which includes 73 amino acids (i.e. in the simulation, we also include the MET amino acids at position 217 used to obtain the NMR structure). We thus simulate a system with 146 amino acids.

To perform extensive simulations, we use a coarse-grained representation of the protein chain coupled with an energy function based on the knowledge of the PDB fibril structure. In the spirit of Go-like approaches widely used for globular proteins,[42] the energy function is built in such a way to have its minimum for the PDB structure. Inspired by Ref. 58, each amino acid is represented by an effective spherical atom located at the position of the corresponding C^α atom. The virtual bond angle associated with three consecutive C^α atoms is constrained between 82° and 148°. Virtual bond lengths are kept constant and equal to the native values from the PDB file. To implement steric constraints, we require that no two nonadjacent C^α atoms are allowed to be at a distance closer than 3.9 Å. Hydrogen bond formation is allowed only between residue pairs that form them in the PDB fibril structure. We assign an energy -1 to each formed hydrogen bond and we disregard any other attractive interaction (i.e. hydrogen bonds cannot be formed by residue pairs that do not form them in the PDB fibril structure and we do not consider any other type of pairwise interaction except for the excluded volume constraints). Only β-sheet stabilizing hydrogen bonds can therefore be formed in our simulation, and to identify them within a C^α-representation, we use the geometrical rules for nonlocal hydrogen bonds introduced in Ref. 58. To recognize the hydrogen bonds present in the PDB fibril structures, the lower bound on the scalar product between binormal and connecting vectors was decreased to 0.88 (0.94 in the original formulation, see Table 1 and Figure 1 in Ref. 58 for the precise listing of all hydrogen bond rules and the definition of binormal and connecting vectors).

In this way, we find in the PDB fibril structure (see Figs. 2 and 3) two long parallel β-strands (β_1 and β_3), connected by nine hydrogen bonds and four shorter strands: β_{2a} parallel to β_{4a} (linked together by four hydrogen bonds) and β_{2b} parallel to β_{4b} (two hydrogen bonds). Those strands alternate within the fibrillar structure in pairs which form hydrogen bonds within the same chain (intrachain bonds) and pairs which form hydrogen bonds between neighboring chains (interchain bonds). Each strand in the core of the fibrillar structure forms intrachain bonds on one side and interchain bonds on the other side. In the "top" side of the fibril (see Fig. 2), the exposed strands in the sticky end are β_3, β_{4a} and

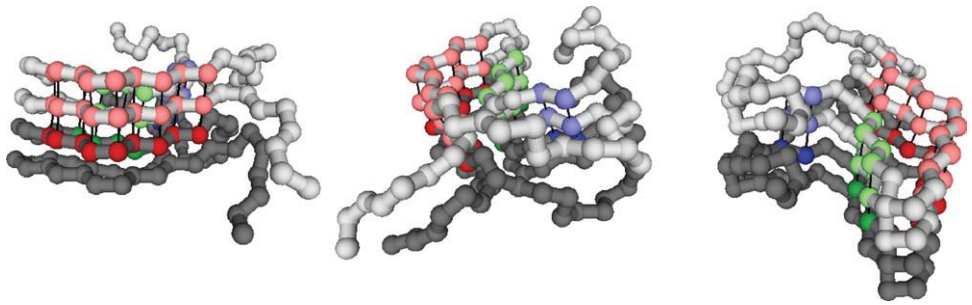

Figure 2

Coarse-grained representation of HET-s molecules (top-side elongation). Different views of the HET-s PFD structure used as the minimum energy structure in our simulations. Chains A and B from the PDB fibril structure are kept. During the simulation of top-side elongation, the light chain is mobile, whereas the dark one is frozen and represents the fibril end to which the mobile chain is attaching. The three types of β-stranded regions are depicted in red (β_1/β_3), green (β_{2a}/β_{4a}), and blue (β_{2b}/β_{4b}). The hydrogen bonds used in the Go-like energy functions are represented by dark lines joining the interacting C^{α} atoms. [Color figure can be viewed in the online issue, which is available at wileyonlinelibrary.com.]

β_{4b}, whereas in the "bottom" side, the exposed strands are β_1 and β_{2a} β_{2b} (see Fig. 3).

Because we keep fixed one chain, the ground state has energy −30 (15 intrachain hydrogen bonds plus 15 interchain hydrogen bonds–we are not counting the intrachain bonds of the frozen chain). Hence, energy can range from 0 (unbound chains) to −30 (fully bound chains in the fibrillar state). To fix a realistic temperature scale, the effective value of hydrogen bond energy in our Go-like energy function was given the value 3.5 kcal mol^{-1}, so that the unit temperature of our simulations corresponds to 1760 K.

We have simulated the elongation of the fibril from both sides. For each side, we simulated chains confined in a hemisphere centered in the origin and of radius L_1 = 5 nm, L_2 = 10 nm, and L_3 = 30 nm corresponding to concentrations c_1 = 6.4 m*M*, c_2 = 0.8 m*M*, and c_3 = 30 μ*M*. The latter value is close to concentrations typical of *in vitro* aggregation experiment.[29,54]

Monte Carlo simulation

Fibril elongation is simulated by a Monte Carlo procedure. Multiple Markov processes,[59] each replicating the same system of a fixed chain and a free chain attaching to it as described above, are run in parallel at different temperatures, with possible swaps of replicas, to sample efficiently the conformational space from high (T = 210°C) to low temperatures (T = 10°C). Within the same replica, conformations are evolved using trial moves, which either pivot a part of the chain from a randomly chosen residue to its end or rotate a chain portion between two residues along the direction joining them. In the latter case, the two residues are either chosen randomly or chosen to be next-nearest neighbors along the chain. Trial moves are accepted or rejected according to the Metropolis test.[60] We use 20 different replicas, choosing their temperatures to sample more accurately the transition region (40°C < T < 100°C) and to provide reasonable overlap of energy histograms between

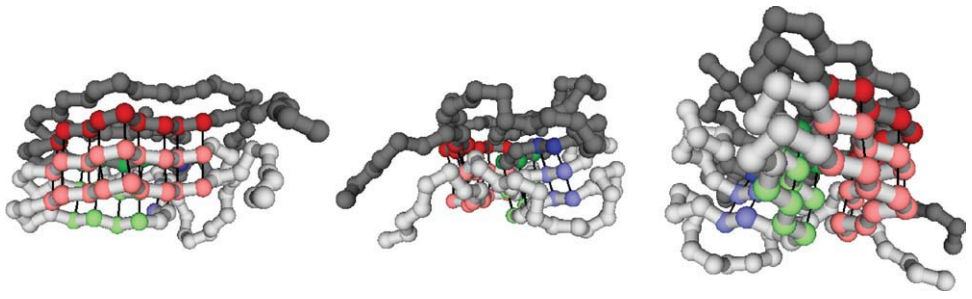

Figure 3

Coarse-grained representation of HET-s molecules (bottom side-elongation). Different views of the HET-s PFD structure used as the minimum energy structure in our simulations. Chains A and B from the PDB fibril structure are kept. Color codes are the same as in Figure 2 and refer to the case of bottom-side elongation. [Color figure can be viewed in the online issue, which is available at wileyonlinelibrary.com.]

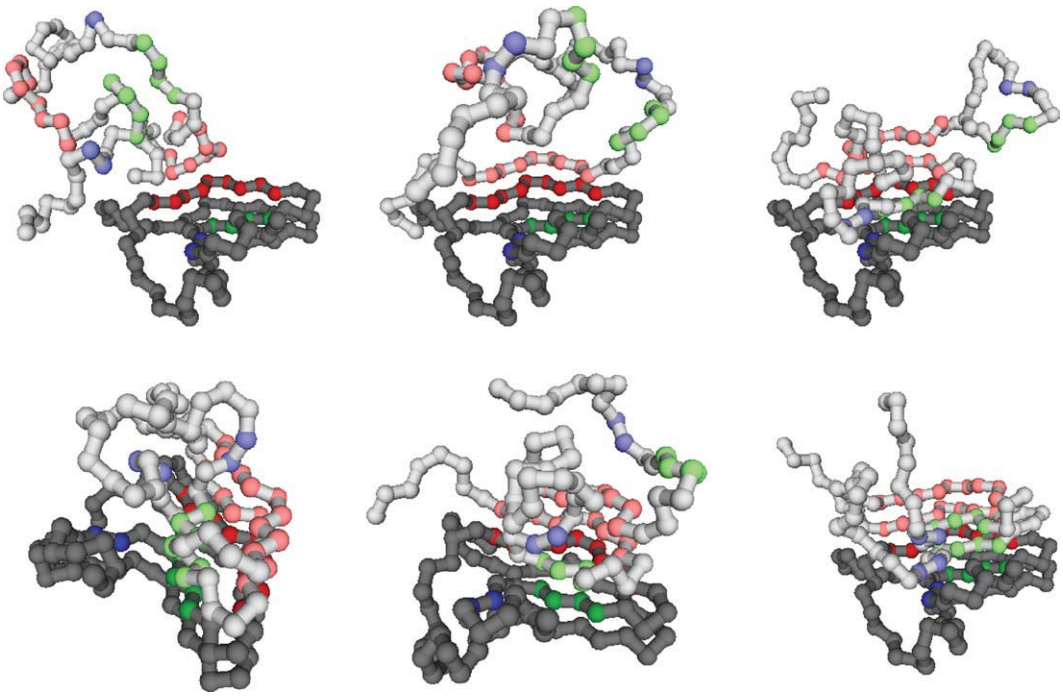

Figure 4

Snapshot conformation from numerical simulations. Some snapshots representing conformations visited during the simulation of fibril elongation from the top side. Color codes are the same as in Figure 2. [Color figure can be viewed in the online issue, which is available at wileyonlinelibrary.com.]

neighboring pairs. Roughly $2N$ Monte Carlo steps (N = 73 is the number of residues of the free chain) are independently performed for each replica before one replica swap is attempted among a randomly chosen neighboring pair. Overall, roughly 10^7 replica swaps are attempted for each simulation and the acceptance rate of replica swaps in all cases is above 60%. The convergence to the equilibrium regime is assessed by looking at the evolution of system energy as a function of Monte Carlo steps. To compute equilibrium thermodynamic averages, the simulation portion corresponding to the initial N_{eq} swaps is discarded from the collected data, with N_{eq} ranging from 1.5×10^6 to 5×10^6, depending on concentration. Data from all temperatures are elaborated with the multiple-histogram method.[61] In Figure 4, some snapshots of the simulations are represented.

RESULTS

Cooperativity of the elongation process

To characterize the thermodynamic properties of the HET-s fibril growth process, we study the behavior of the energy and heat capacity of the system as a function of the temperature for three different protein concentrations (see Fig. 5) and by considering elongation from both the top and the bottom side (see the Methods Section). The peaks in the heat capacity curve signal the occurrence of large conformational rearrangements (strictly speaking that would become transitions only in the thermodynamic limit of the number of system component going to infinite) related to the process of the deposition of the free HET-s PFD chain to the one that is kept fixed to represent the sticky end of the already formed fibril.

As expected, the first association temperature, related to the high-temperature heat capacity peak, decreases when decreasing the concentration. It reaches values close to room temperature for the concentration c_3 = 30 μM. Interestingly, the cooperativity of the transition increases for lower concentrations: this is signaled by a more sigmoidal behavior of the energy profiles, by the sharpening of heat capacity peaks and by the almost complete merging in one single narrow peak of the otherwise complex peak structure. At a first glance, despite the growth processes from the two different sides look similar, one can notice that at low concentration, a residual peak remains at low temperature for the top elongation case.

Stability of hydrogen bond formation

To elucidate these behaviors further and to understand the nature of the conformational rearrangements related to heat capacity peaks, we computed the formation prob-

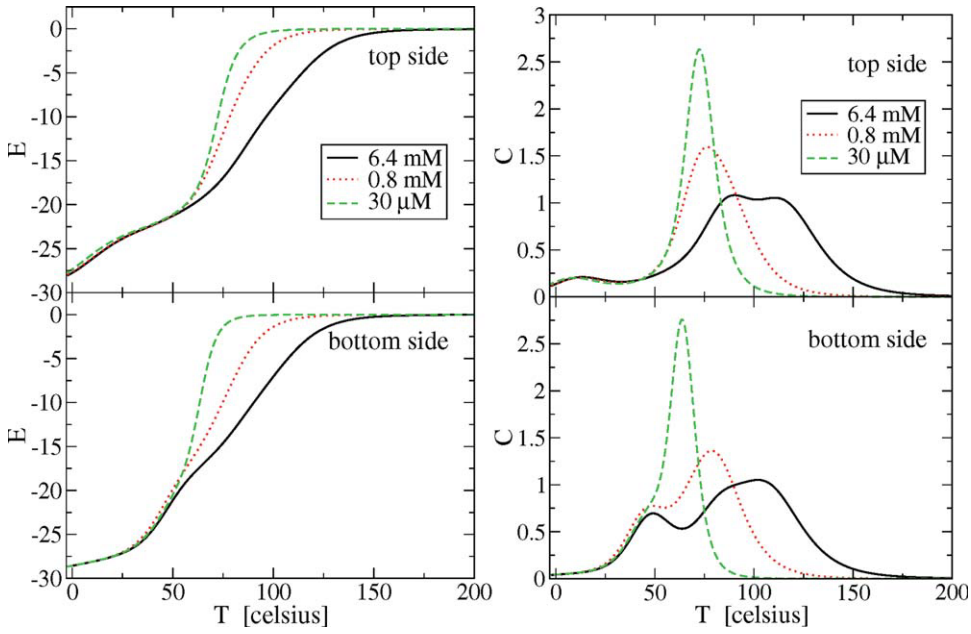

Figure 5

Energy and heat capacity curves. Energy E and heat capacity $C = dE/dT$ as a function of temperature $T(^\circ C)$, for both elongation sides and three different concentrations c_1, c_2, and c_3 used in this work. Both E and C are plotted in simulation units so that one energy unit (minus one hydrogen bond) corresponds to 3.5 kcal mol^{-1} (see the Methods section), whereas one heat capacity unit corresponds to the gas constant $R = 1.99 \times 10^{-3}$ kcal mol^{-1} K^{-1}. [Color figure can be viewed in the online issue, which is available at wileyonlinelibrary.com.]

ability of hydrogen bonds for the different strands as a function of temperature (shown in Fig. 6). We define the stabilization temperature of a group of hydrogen bonds to correspond to their average formation probability at thermodynamic equilibrium being equal to 0.5. We compute stabilization temperatures for six possible groups of hydrogen bonds, corresponding to the different strand pairings shown as separate white/black bands in Figure 6. The resulting stabilization temperatures are summarized in Table I.

We will use the term "fibrillar" for interchain hydrogen bonds. As an example, strand β_1 of the mobile chain couples with strand β_3 of the fixed chain, in the case of elongation from the top side, whereas strand β_3 of the mobile chain couples with strand β_1 of the fixed chain in the case of elongation from the bottom side, and similarly for other strand pairs (see Fig. 6 caption for a detailed explanation of how intrachain and fibrillar hydrogen bonds are represented in the figure).

For all concentrations and both elongation sides, the first hydrogen bonds which become stable are the interchain ones formed between the long strands β_1 and β_3, at a temperature T_{f13} varying from 115°C for top elongation at concentration c_1, to 65°C for bottom elongation at c_3 (see Table I). The stabilization temperature T_{f13} of fibrillar hydrogen bonds between the long strands is higher for higher concentrations and, at the same concentration, for the case of top-side elongation.

This first stabilization process is followed at a lower temperature T_{i13} (varying from 85°C for top elongation at concentration c_1, to 63°C for bottom elongation at c_3, see Table I) by the stabilization of intrachain hydrogen bonds formed between the two long strands, β_1 and β_3, of the mobile chain. This second stabilization temperature is again higher for the top elongation case, at the same concentration, and increases with concentration.

With a further decrease of the temperature, the fibrillar hydrogen bonds formed between the short strands (β_{2a} with β_{4a} and β_{2b} with β_{4b}) become stable. The stabilization temperature T_{f24a} for interchain strand pair β_{2a} and β_{4a} does not depend on concentration but only on the elongation side, being higher, $T_{f24a} \simeq 63^\circ C$, for top elongation with respect to $T_{f24a} \simeq 50^\circ C$ for bottom elongation. The stabilization temperature T_{f24b} for interchain strand pair β_{2b} and β_{4b} is roughly the same, $T_{f24b} \simeq 42$–$43^\circ C$, in all cases.

The last step involves the stabilization of the intrachain hydrogen bonds between the short strands and do not depend on concentration as well. At this stage, the more significant difference between the two elongation sides emerges. For top-side elongation, the two short strand pairs are stabilized roughly together at a temperature much lower with respect to the previous step ($T_{i24a} \simeq 10^\circ C$ corresponding to the small peak in the heat capacity curve and $T_{i24b} \simeq -2^\circ C$). For bottom-side elongation, the stabilization of the two short intrachain

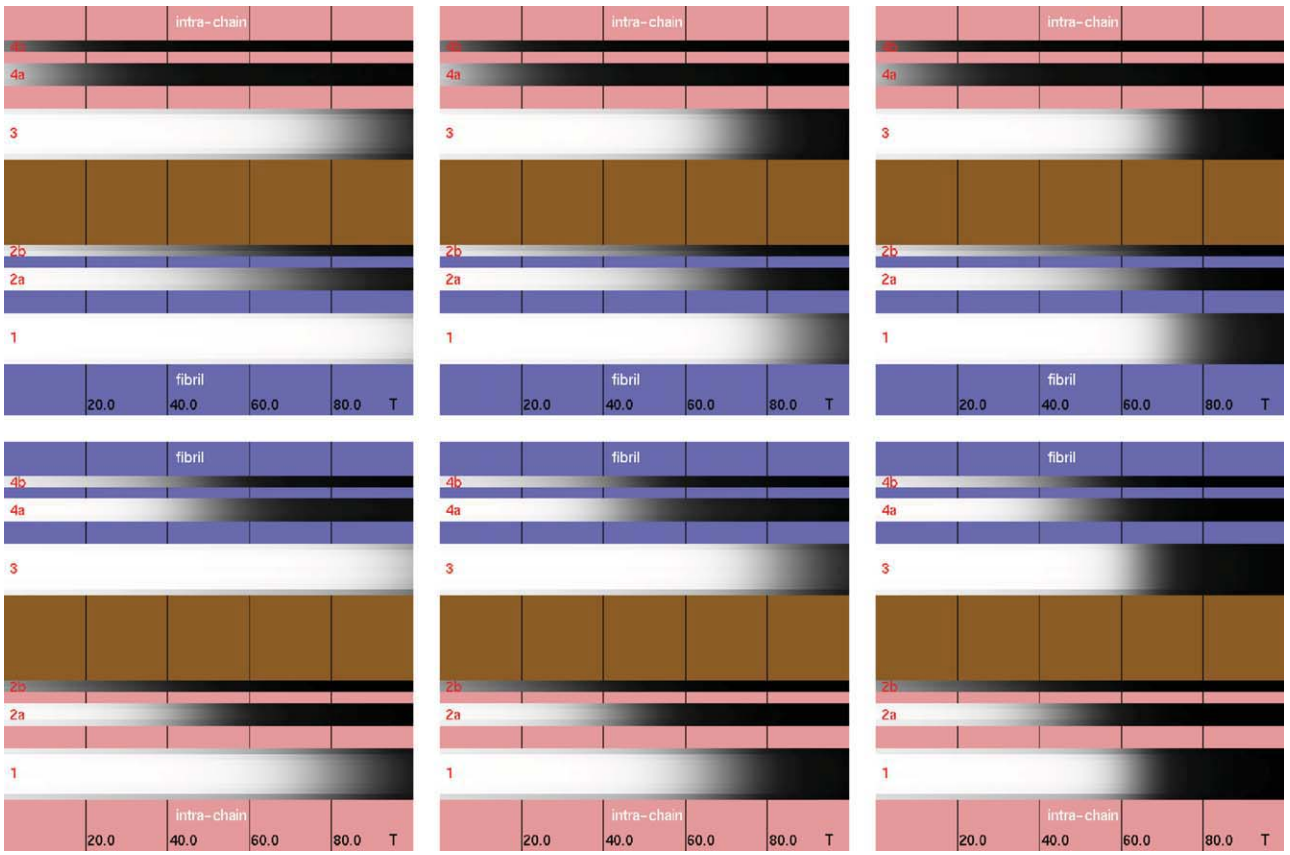

Figure 6

Hydrogen bond formation probabilities. Plots of hydrogen bond formation probabilities in the mobile chain as a function of temperature $T(^{\circ}C)$, for top-side elongation (upper row) and bottom-side elongation (lower row); columns refer to the three different concentrations c_1 (left), c_2 (middle), and c_3 (right) used in this work. White refers to bonds formed with probability 1; black to bonds never formed. We use a representation in which hydrogen bonds formed between two residues are ascribed to the more "external" residue of the two, according to the direction defined by fibril elongation. In all plots, this residue index is represented on the *y*-axis, from the N-terminus to the C-terminus. The lower wide black/white band corresponds to residues in the strand β_1 (nine hydrogen bonds), followed by residues in β_{2a} (four hydrogen bonds) and β_{2b} (two hydrogen bonds), and again residues in β_3 (nine hydrogen bonds), followed by residues in β_{4a} (four hydrogen bonds) and in β_{4b} (two hydrogen bonds). Strands are then divided into two larger groups, according to the nature of the associated hydrogen bonds, which may form intra chain (pink band) or inter chain (fibrillar blue band). The assignment of strands to the two groups depends on the elongation side. For instance, for top-side elongation (upper row), strand β_1 of the mobile chain is on the "internal" fibrillar side of the chain and the associated hydrogen bonds form inter chain, with the strand β_3 of the fixed molecule. On the other hand, for bottom-side elongation (lower row), strand β_1 of the mobile chain is on the "external" exposed side of the molecule and the associated hydrogen bonds form intra chain, with the strand β_3 of the same molecule. The brown band corresponds to the loop (246–260) separating the two groups of strands. [Color figure can be viewed in the online issue, which is available at wileyonlinelibrary.com.]

strand pairs takes place at quite different temperatures: hydrogen bonds between strands β_{2a} and β_{4a} are stabilized at a slightly even higher temperature than their interchain counterpart ($T_{i24a} \simeq 44^{\circ}C$), whereas the intrachain strand pair β_{2b} and β_{4b} is stabilized at a much lower temperature ($T_{i24b} \simeq 6^{\circ}C$).

Dock and lock mechanism

On assuming that the order in hydrogen bond stabilization mirrors a similar order in the kinetics of the elongation process, we can extract a general message from these results by stating that the attaching of a mobile chain onto the elongating fibril is triggered by the formation of the interchain hydrogen bonds of the longest strand (β_1 or β_3) followed by a first partial folding of the chain through the formation of the long intrachain strand pair (between β_1 and β_3) and by the successive formation of all other interchain and intrachain hydrogen bonds. The mechanism of the addition of a soluble unstructured monomer to a preformed ordered amyloid fibril is a complex process: the deposition involves an association of the unstructured monomer to the fibril surface (docking) followed by a conformational rearrangement leading to the incorporation onto the underlying fibril lattice (locking).[18,24–26]

Table I
Stabilization Temperatures of Hydrogen Bond Groups for the Different Concentrations and Elongation Modes Used in Our Simulations

	T_{f13} (°C)	T_{i13} (°C)	T_{f24a} (°C)	T_{f24b} (°C)	T_{i24a} (°C)	T_{i24b} (°C)
Top-side elongation						
c_1	115	85	64	43	12	−1
c_2	88	71	63	44	11	−2
c_3	75	70	62	43	8	−3
Bottom-side elongation						
c_1	108	80	50	42	45	6
c_2	85	68	47	40	43	7
c_3	65	63	50	41	44	6

Hydrogen bonds stabilizing a given strand pair are grouped into the same set, resulting into six different sets (see Fig. 6 caption for a detailed explanation). Stabilization temperatures for different sets are labeled in such a way that, for example, T_{f13} (T_{i24a}) refers to fibrillar (intrachain) hydrogen bonds formed between strands β_1 and β_3 (β_{2a} and β_{4a}).

We identify the docking stage with the formation of both interchain and intrachain hydrogen bonds between the long strands β_1 and β_3, as in both cases, the stabilization temperatures T_{f13} and T_{i13} depend on concentration (see Table I). One indeed expects that in a denser regime, it is easier for the mobile chain to dock onto the fibril end, while the locking into the β-helix structure necessary for fibril propagation should not be affected by concentration changes. Therefore, the locking stage involves the formation of both interchain and intrachain hydrogen bonds between the remaining shorter strands, as we observe that their stabilization temperatures do not depend on concentration. The dependence of the intrachain hydrogen bond stabilization temperature T_{i13} on concentration is nontrivial and is triggered by the strong concentration dependence of the formation probability of the fibrillar hydrogen bonds between the long strands. The higher the concentration, the more probable the fibrillar bonds to be formed. Consequently, the more easily the intrachain bonds are stabilized.

From the data shown in Figure 6 and in Table I, another general feature can be picked out: the temperature range in which the docking stage and thus the full elongation process take place decreases at lower concentrations. This is consistent with the increment of cooperativity as it appears from thermodynamic quantities (e.g. sharpness of heat capacity peaks in Fig. 5) when concentration diminishes. The most cooperative behavior, as

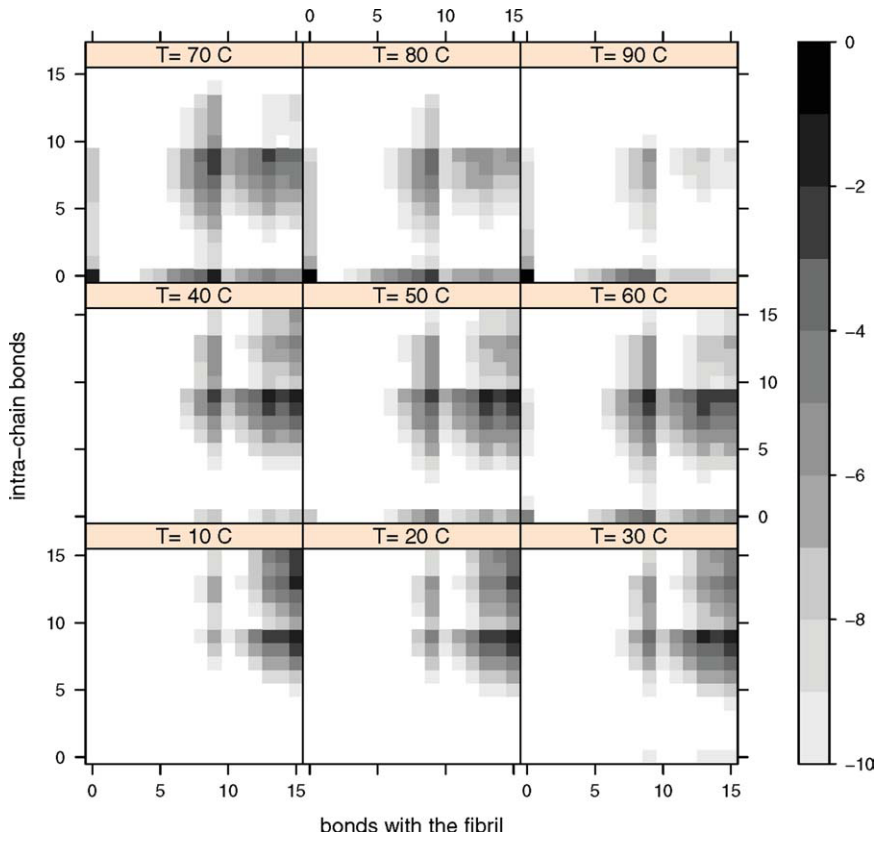

Figure 7
Equilibrium occupation probabilities of macroscopic conformational states. Equilibrium occupation probability of conformational states, in logarithmic scale, shown for different temperatures T (°C), at concentration c_3 in the case of growth from the top side. Macroscopic states are defined according to the number of formed fibrillar and intra chain hydrogen bonds, which are shown in the axes of each plot. The darker (lighter) the color, the higher (smaller) the probability to occupy the corresponding macroscopic state. The numbers in logarithmic scale may be interpreted as the opposite of free energies in RT units. [Color figure can be viewed in the online issue, which is available at wileyonlinelibrary.com.]

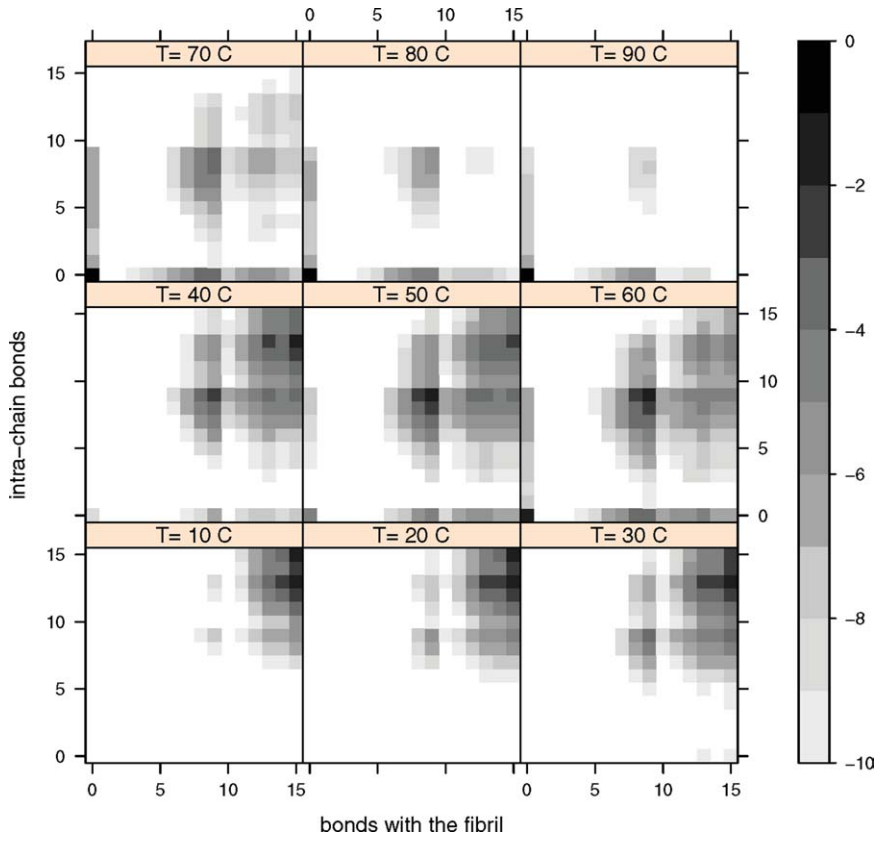

Figure 8

Equilibrium occupation probabilities of macroscopic conformational states. As in Figure 7, in the case of growth from the bottom side. [Color figure can be viewed in the online issue, which is available at wileyonlinelibrary.com.]

shown by the presence of a single sharp peak in the heat capacity curve, is obtained at concentration c_3 in the case of bottom-side elongation, whereas a second peak is clearly visible at low temperature for top-side elongation at the same concentration. The above analysis of Figure 6 data reveals the crucial role of the formation of intrachain hydrogen bonds between strands β_{2a} and β_{4a} in this respect. The stabilization temperature T_{i24a} of these hydrogen bonds constitutes the most relevant difference between the two elongation modes in the first place. Moreover, it does correspond closely in both cases to significant features in the heat capacity curve, namely the small peak at $T_{i24a} \simeq 10^{\circ}$C for top elongation and the small shoulder in the main peak at $T_{i24a} \simeq 44^{\circ}$C for bottom elongation.

Competition between intrachain and interchain hydrogen bonds

To gain a further understanding of the role played by intrachain β_{2a}–β_{4a} hydrogen bonds, we computed the equilibrium occupation probabilities of macroscopic conformational states, which are defined according to the number of formed intrachain and interchain hydrogen bonds. In Figures 7 and 8, the results are shown at different temperatures, for concentration c_3 and two different growth modes. Occupation probabilities are shown in logarithmic scale, so that the resulting data could be interpreted as (the opposite of) effective free energies or mean force potentials. At high temperature, the bottom left corner is mostly populated, corresponding to conformations with very few or none intrachain and interchain hydrogen bonds formed, typical of a mobile chain not yet attached to the fibril end. On the other hand, at very low temperature, the opposite top right corner is populated, describing structures with almost all the hydrogen bonds formed that correspond to mobile chains found already completely associated with the fibril end with a significant probability.

Consistently with the previous analysis, based on Figure 6 data, the elongation process is complex, taking place in several stages. Macrostates with only intrachain hydrogen bonds are found to be populated to some extent at high temperatures, hinting to the possibility of a prestructuring of the mobile chain before docking to the fibril tip, yet the pathway more significantly visited

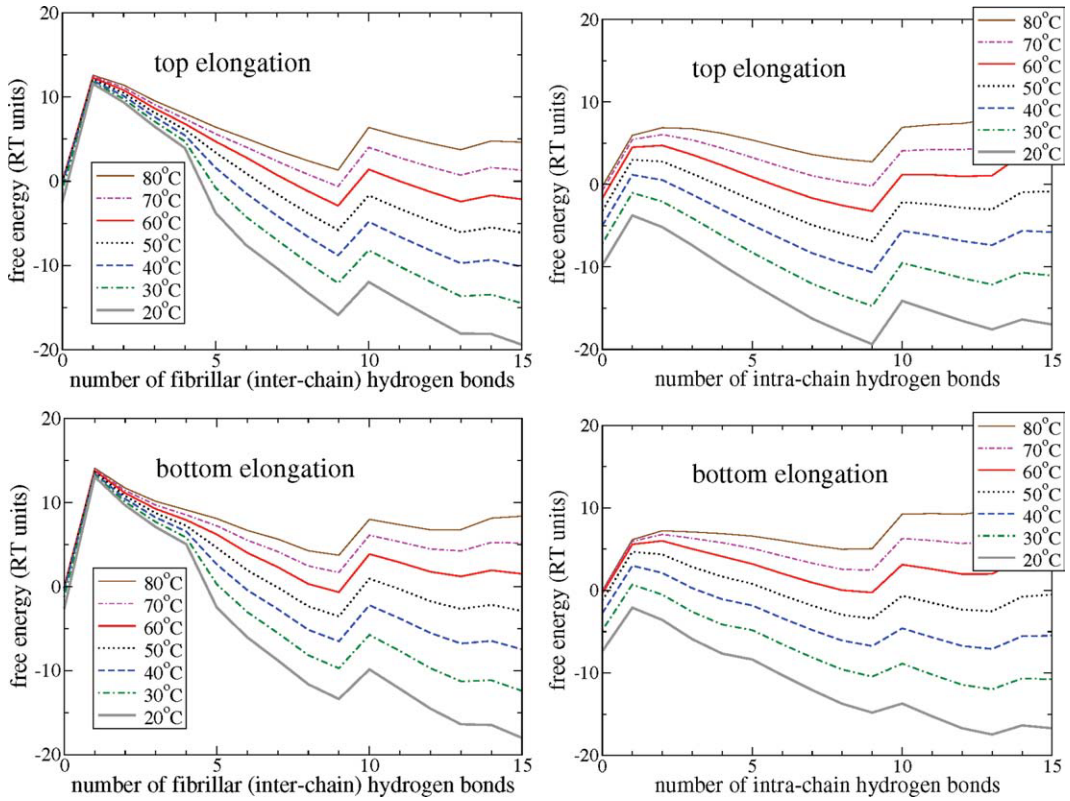

Figure 9

Unidimensional energy profiles. Adimensional free energy profiles (in *RT* units), as a function of either the number of inter chain fibrillar hydrogen bonds (left panels) or the number of intra chain hydrogen bonds (right panels). Different profiles are shown for different temperatures in each panel, and both elongation modes are considered for the case of concentration c_3 : top elongation in the upper panels and bottom elongation in the lower panels.

involves the population of first nine fibrillar hydrogen bonds between strands β_1 and β_3 and then the analogous intrachain bonds (see $T = 70^{\circ}$C in Figs. 7 and 8).

After this first stage, that we already identified with docking, two different scenarios again clearly emerge depending on the growth mode. The overall process is visibly more cooperative for bottom-side elongation (Fig. 8) with respect to top-side elongation (Fig. 7), as the spreading of significantly visited macrostates is restricted to a narrower temperature range in the former case. Moreover, around room temperature ($T = 20$–30°C), the most populated state for bottom-side elongation has 15 fibrillar and 13 intrachain hydrogen bonds formed corresponding to a chain almost completely attached to the fibril end (only strand β_{2b} is left wiggling a bit). Instead, the most populated state for top-side elongation has all 15 interchain but only nine intrachain hydrogen bonds locked into the fibrillar conformation, signaling again that the stability of intrachain β_{2a}–β_{4a} hydrogen bonds is strongly weakened with respect to bottom-side elongation.

To appreciate more easily the variations with temperature in the population of the different macrostates, we computed unidimensional free energy profiles as a function of the number of either intrachain or interchain hydrogen bonds. The results are shown in Figure 9 for concentration c_3 and two different growth modes.

Figure 9 confirms the multistage nature of the association process with different macrostates that become the global free energy minimum at different temperatures. The free energy profiles as a function of the number of fibrillar hydrogen bonds are similar in both elongation modes. The main difference is the value of the temperature below which the free state (none fibrillar hydrogen bond is formed) is not the free energy minimum anymore: 70°C for top elongation and 60°C for bottom elongation, consistently with Table I.

The free energy of the free state and the free energy barrier that separates it from the competing minimum with nine fibrillar bonds (the ones formed between the β-strands β_1 and β_3 that are the first to be stabilized in the association process) do not basically depend on temperature. This is a signature of their entropic origin (free energies in Fig. 9 are plotted in *RT* units), as they are dominated by the rototranslational entropy of the free chain.

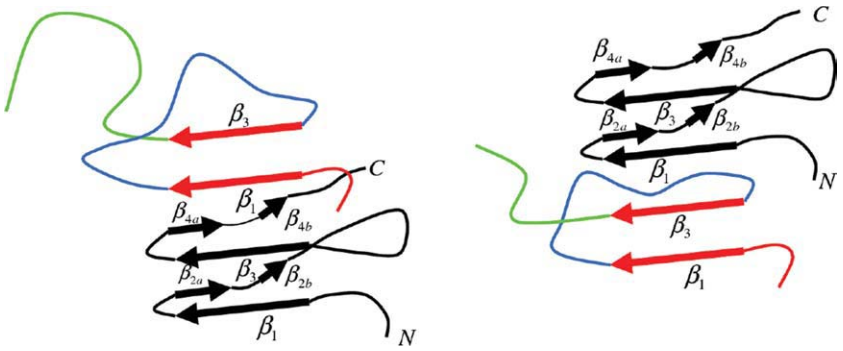

Figure 10

Fibril growth polarity caused by topological properties. Cartoon representation of the elongating fibril after the initial docking of the attaching mobile chain (in colors) onto the fixed chain (in black, it represents the tip of the fibril) has just taken place and before the final locking stage. Only β-strands already formed are shown, in red for the mobile chain (the long strands). The remaining fluctuating portions of the mobile chain are shown in green (the tail) and in blue (the loop). Right: top-side elongation. Left: bottom-side elongation. [Color figure can be viewed in the online issue, which is available at wileyonlinelibrary.com.]

On the other hand, the free energy profiles as a function of the number of intrachain hydrogen bonds display a relevant difference between the two elongation modes, consistently with previous observations. For top elongation, the free energy minimum at $T = 20^{\circ}C$ is the macrostate with only nine intrachain hydrogen bonds (i.e. the β-strands β_{2a} and β_{4a} are not yet paired), whereas for bottom elongation, the free energy minimum at $T = 20^{\circ}C$ is the macrostate with 13 intrachain hydrogen bonds (i.e. the β-strands β_{2a} and β_{4a} are already paired).

Interestingly, the above difference is due to the macrostate with nine intrachain hydrogen bonds being entropically stabilized for top elongation with respect to bottom elongation. Indeed, the free energies for 10–15 intrachain hydrogen bonds do not differ in the two elongation modes. Moreover, the free energy difference between the two elongation modes for nine intrachain hydrogen bonds has to be entropic, as the energy of that macrostate is the same in both cases, being given by the nine intrachain plus the 15 interchain hydrogen bonds (the latter is the global free energy minimum at $T = 20^{\circ}C$ for both elongation modes).

Topological origin of fibril growth polarity

Our analysis clearly established that fibril growth exhibits a deeply different thermodynamic behavior depending on the side from which elongation proceeds: at room temperature only bottom-side elongation is thermodynamically stable. What is the physical reason for the existence of such a strong growth polarity? Because our simulation study is based only on the knowledge of the fibril structure and not on the specificity of the amino acid sequence, we can expect that growth polarity is a consequence of the topological properties of the structure.

There is indeed a deep topological difference between the deposition mechanisms of HET-s PFD on the two different sides of the fibril. In the first docking stage, common to both elongation modes, the formation of both interchain and intrachain hydrogen bonds between β_1 and β_3 implies the positioning of the latter strands into a conformation already compatible with the final fibrillar structure. The remaining strands, then, yet to be positioned, acquire distinct topological roles, as β_{2a} and β_{2b} are in a loop between the two chain portions already pinned down in the fibrillar structure, whereas β_{4a} and β_{4b} are in the C-terminal tail of the chain. One can then predict that, for entropic reasons, the former pair can be accommodated into the final fibrillar structure more easily than the latter pair. Nevertheless, different elongation modes may change this hierarchy.

When elongation proceeds from the top side, the attaching chain wraps up onto the fibril tip starting with its N-terminal part (see Fig. 10). The "loop" strands β_{2a} and β_{2b} (fibrillar) need to be positioned before the "tail" ones β_{4a} and β_{4b} (intrachain), consistently with the above-suggested topological order. Indeed we do observe this hierarchy for top-side elongation; even at low temperature, intrachain hydrogen bonds between the short strand pairs are not yet stable.

When elongation proceeds from the bottom side, the attaching chain wraps up onto the fibril tip starting with the C-terminal part (see Fig. 10). The "tail" strands β_{4a} and β_{4b} (fibrillar) now need to be positioned before the "loop" ones β_{2a} and β_{2b} (intrachain). Elongation order takes over the topological order so that the difficult positioning of "tail" strands is assisted by the easier positioning of "loop" strands and both are stabilized at room temperature (with the partial exception of the shortest strand β_{2b}).

DISCUSSION

In this work, we have used Monte Carlo simulations of a coarse-grained representation of HET-s PFD to study the elongation of the corresponding amyloid fibril. More specifically, we described how a mobile chain gets attached to a prefixed fibrillar structure. Our approach, based on the knowledge of the fibrillar structure, relies on the currently well-accepted assumption that protein topology plays a pivotal factor in determining unimolecular folding and protein assembly. At variance with other Go-like studies,[51,52] based on a hypothetical structure, the reliability of our study is justified by the knowledge of a high-resolution NMR structure of a plausibly functional amyloid fibril.

There are two main results of our thermodynamic study. First, we observe that fibril elongation is driven by the formation of interchain and intrachain hydrogen bonds between the long strands β_1 and β_3, followed by the positioning of the rest of the attaching chain onto the growing fibril. This mechanism is known as dock and lock mechanism.[18,24] We identify the docking stage as the part of the association process whose onset temperature displays a concentration dependence. A similar feature, that is the range of the docking temperature varies with concentration, was previously found in a thermodynamic study of Aβ-peptide fibril growth.[27] Within our Go-like approach, we find a complex multistage association process, where both the docking and the locking stages proceed in several steps in a free energy landscape characterized by several different minima separated by barriers. In the case of Aβ-peptide fibril elongation, it was found on the contrary that docking is continuous and proceeds without the presence of intermediate or free energy barriers.[27] Our finding of a multistage docking behavior might be due to the nontrivial intrachain topology of HET-s PFD monomer, lacking in the Aβ-peptide case. Alternatively, it might be an artifact caused by our neglecting of non-native interactions.

Second, we predict that one side of the structure is more suitable to sustain the growth of the fibril.

The predicted fibril growth polarity can be rationalized by analyzing elongation topological properties, which turn out to be intrinsically different from the two fibril sides. The argument is based on the complex tertiary structure of the monomeric unit within HET-s fibril, resulting into alternating intrachain and interchain pairs of β-strands. After the first hydrogen bonds have been formed in the initial docking onto the growing fibril, the portion of the attaching chain, which is going to acquire β-structure in the following locking stage, is partitioned into a loop and a tail part (see Fig. 10). As a consequence, the entropy loss of the two parts on locking is different, implying a "topological" hierarchy. The latter may or may not be affected by the "winding" hierarchy dictated by the choice of the growth side, thus resulting in a strong growth polarity. Bottom-side elongation is more sustainable because the loop part may assist the tail part to lock. The entropic origin of the growth polarity observed in our results is further confirmed by the free energy profiles as shown in Figure 9. As discussed in the "Competition between intrachain and interchain hydrogen bonds" section, the macrostate populated after docking and before locking (with 15 interchain and nine intrachain hydrogen bonds) is entropically stabilized in the top elongation mode with respect to bottom elongation.

Being based on a topological argument, we believe our prediction to be robust against both variations of the details in the implementation of our Go-like approach (changing the coarse graining of protein chain representation, using not only hydrogen bonds but also general pairwise contacts in the energy function, and using different hydrogen bond rules) and relaxation of other simplifying assumptions that we made, namely the fibril tip is represented by just one chain and kept completely frozen. This latter point is further motivated by the experimental observation[29] that the HET-s fibril accommodates incoming prion monomers without a substantial disorganization of its structure. This behavior is quite different from those of Aβ fibrils where it was experimentally observed[62] an entropy gain in the elongation reaction which was related to an unfolding of the organized fibril end to accommodate the addition of the incoming monomers.

We thus suggest our prediction may be accessible to experimental validation, for instance using the single fiber growth assay used in Ref. 56 for SUP35 yeast prion, based on two variants of the prion domain that can be differentially labeled and distinguished by atomic force microscopy.

The same topological argument cannot be used for simpler amyloid structure such as the solid-state NMR model suggested for the Alzheimer's Aβ-peptide,[63] in the absence of intrachain hydrogen bonds. In fact, experimental evidence shows bidirectional fibril growth with no clear signs of growth polarity.[55] Interestingly, the presence of asymmetrical topological properties of fibril ends was indeed suggested for the Aβ-peptide,[27,57] depending on the different possible quaternary arrangements of the fibril.[64] On the other hand, a clear evidence of growth polarity was demonstrated for SUP35 fibrils,[56] a yeast prion protein believed to have a functional role, similarly to HET-s prion. There is no high-resolution information on the structure of SUP35 fibrils and different conflicting structural models have been recently proposed,[65,66] yet some of the available data suggest the existence of a complex intrachain structure,[67] which could justify the observed growth polarity within a framework similar to the one we propose here for HET-s.

A peculiar feature of HET-s PFD is the presence of a long loop in the fibrillar structure that connects strands

β_{2b} and β_3 (aa 246–260), which then contributes to increasing the length of the chain portion partitioned as loop in the topological argument discussed above (blue in Fig. 10). An interesting question is whether increasing such length favors or disfavors growth polarity according to the mechanism suggested here. One could argue that a longer loop may further decrease the fluctuations available to the tail part, thus enhancing its assisted locking for bottom-side elongation. Indeed, it is known that a large deletion in such loop (248–256) led to loss of HET-s function and infectivity.[9] Even though no evidence is known about the possible biological relevance of fibril growth polarity in fungal and yeast prions, it is tempting to speculate that the role of the loop might be to enhance growth polarity as a way to control the elongation process more thoroughly in the context of the propagation of a functional prion. Numerical simulations performed within the same Go-like approach, based on a model structure to be built on the basis of HET-s PFD but with a shorter loop, will shed further light on this hypothesis.

Our coarse-grained approach turned out to be effective in studying structural rearrangements which could not be tackled using more detailed protein chain representations. On the other hand, we are neglecting factors which may play an important role in the elongation process, such as the possible presence of oligomeric conformers of HET-s PFD in the nonfibrillar soluble state.[29] To capture similar effects, one needs to increase the accuracy of the energy function by introducing amino acid specificity. This can be done by using coarse-grained potentials which take into account the different ability of each pair of amino acids in forming hydrogen bonds in β-strands,[68,69] coupled with similar potentials describing residue pairwise interactions[70] or local conformational biases.[71] Such potentials might be used to modulate the Go-like energy function presented in this work. The use of a more realistic description of the protein chain involving side-chain atoms may also cause the amino acid sequence to affect the elongation process in a side-depending manner by imposing chiral stereochemical constraints. The latter are not present in our C^{α}-based representation, thus reinforcing the topological origin of growth polarity in our results.

Finally, the approach presented here could be also used to study the nucleation process of HET-s PFD, and further extended to study the aggregation of the full HET-s protein. The HET-s N-terminal domain in the nonfibrillar soluble form is structured into a globular protein fold whose high-resolution structure has been very recently released[54] (PDB code 2wvn.pdb). Such structure is known to lose partially its order on ordering and aggregation of HET-s PFD into the unsoluble fibrillar form.[72] A Go-like approach would be especially suited to study the resulting competition between the ordered structures of the two domains in the two different forms.[73]

ACKNOWLEDGMENTS

The authors thank F. Chiti and R. Riek for enlightening discussions.

REFERENCES

1. Aguzzi A, Sigurdson C, Heikenwaelder M. Molecular mechanisms of prion pathogenesis. Annu Rev Phatol 2008;3:11–40.
2. Prusiner SB. Novel proteinaceous infectious particles cause scrapie. Science 1982;216:136–144.
3. Wells GAH, Scott AC, Johnson CT, Gunnig RF, Hancock RD, Jeffrey M, Dawson M, Bradley R. A novel progressive spongiform encephalopathy in cattle. Vet Rec 1987;121:419–420.
4. Will RG, Ironside JW, Zeidler M, Cousens SN, Estibiero K, Alperovitch A, Poser S, Pocchiari M, Hofman A, Smith PG. A novel progressive spongiform encephalopathy in cattle. Lancet 1996;347:921–925.
5. Tuite MF, Serio TR. The prion hypothesis: from biological anomaly to basic regulatory mechanism. Nat Rev Mol Cell Biol 2010;11:823–833.
6. Lange A, Meier B. Fungal prion proteins studied by solid-state NMR. Comptes Rendue Chemie 2008;11:332–339.
7. Saupe SJ. Fungal prion proteins studied by solid-state NMR. Microbiol Mol Biol Rev 2000;64:489–502.
8. Baulgerie A, Dos Reis S, Ritter C, Coulary-Salin B, Chaignepain S, Forge V, Bathany K, Lascu I, Schmitter JM, Riek R, Saupe SJ. Domain organization and structure–function relationship of the HET-s prion protein of *Podospora anserina*. EMBO J 2003;22:2071–2081.
9. Ritter C, Maddelein ML, Simmer AB, Luhrs T, Ernst M, Meier BH, Saupe SJ, Riek R. Correlation of structural elements and infectivity of the HET-s prion. Nature 2005;435:844–848.
10. Wasmer C, Lange A, Van Melckebe H, Siemer AB, Riek R, Meier BH. Amyloid fibrils of the HET-s (218–289) prion form a beta solenoid with a triangular hydrophobic core. Science 2008;319:1523–1526.
11. Castellani F, van Rossum B, Diehl A, Schubert M, Rehbein K, Oschkinat H. Structure of a protein determined by solid-state magic-angle-spinning NMR spectroscopy. Nature 2002;420:98–102.
12. Lange A, Becker S, Seidel K, Giller K, Pongs O, Baldus M. A concept for rapid protein-structure determination by solid-state NMR spectroscopy. Angew Chem Int Ed 2005;44:2441–2444.
13. Baumketner A, Shea JE. The structure of the alzheimer amyloid beta 10–35 peptide probed through replica exchange molecular dynamics simulations in explicit solvent. J Mol Biol 2007;366:275–285.
14. Buchete NV, Hummer G. Structure and dynamics of parallel beta-sheets, hydrophobic core, and loops in Alzheimer's a beta fibrils. Biophys J 2007;92:3032–3039.
15. Cecchini M, Curcio R, Pappalardo M, Mekl R, Caflisch A. A molecular dynamics approach to the structural characterization of amyloid aggregation. J Mol Biol 2006;357:1306–1321.
16. Huet A, Derremaux B. Impact of the mutation A21g (flemish variant) on Alzheimer's beta-amyloid dimers by molecular dynamics simulations. Biophys J 2006;91:3829–3840.
17. Ma BY, Nussinov R. Simulations as analytical tools to understand protein aggregation and predict amyloid conformation. Curr Opin Chem Biol 2006;10:445–452.
18. O'Brien EP, Okamoto Y, Straub JE, Brooks BR, Thirumalai D. Thermodynamic perspective on the dock–lock growth mechanism of amyloid fibrils. J Phys Chem B 2009;113:14421–14430.
19. Tarus B, Straub JE, Thirumalai D. Dynamics of asp23-lys28 salt bridge formation in a beta (10–35) monomers. J Am Chem Soc 2006;128:16159–16168.

20. Reddy G, Straubb JE, Thirumalai D. Dynamics of locking and peptides onto growing amyloid fibrils. Proc Natl Acad Sci USA 2009;106:11948–11953.
21. Takeda T, Klimov DK. Computational backbone mutagenesis of the Aβ peptides: probing the role of backbone hydrogen bonds in aggregation. J Phys Chem B 2010;114:4755–4762.
22. Wei G, Jewett AI, Shea JE. Structural diversity of dimers of the Alzheimer amyloid β (25–35) peptide and polymorphism of the resulting fibrils. Phys Chem Chem Phys 2010;12:3622–3629.
23. Hardy J, Selkoe DJ. The amyloid hypothesis of Alzheimer's disease: progress and problems on the road of therapeutics. Science 2002;297:353–356.
24. Esler WP, Stimson ER, Vinters HV, Jennings JJ, Ghilardi JR, Lee JP, Mantyh PW, Maggio JE. Alzheimer's disease amyloid propagation by a template dependent dock–lock mechanism. Biochemistry 2000;39:6288–6295.
25. Cannon M, Williams A, Wetzel R, Myszka D. Kinetic analysis of beta-amyloid fibril elongation. Anal Biochem 2004;328:67–75.
26. Straub JE, Thirumalai D. Principles governing oligomer formation in amyloidogenic peptides. Curr Opin Struct Biol 2010; 20:187–195.
27. Takeda T, Klimov DK. Replica exchange simulations of the thermodynamics of Aβ fibrils growth. Biophys J 2009;96:442–452.
28. Lange A, Gattin Z, van Meleckebeke H, Wasmer C, Soragni A, van Gunsteren WF, Meier BH. A combined solid-state NMR and MD characterization of the stability and dynamics of the HET-s (218–289) prion in its amyloid conformation. ChemBioChem 2009;10:1657–1665.
29. Sabaté R, Castillo V, Espargaró A, Saupe SV, Ventura S. Energy barriers for HET's prion forming domain amyloid formation. FEBS J 2009;276:5053–5064.
30. Auer S, Kashiev D. Insight into the correlation between lag time and aggregation rate in the kinetics of protein aggregation. Proteins: Struct Funct Bioinf 2010;78:2412–2416.
31. Auer S, Trovato A, Vendruscolo M. A condensation-ordering mechanism in nanoparticle-catalyzed peptide aggregation. PLoS Comput Biol 2009;5:e1000458.
32. Hoang TX, Marsella L, Trovato A, Seno F, Banavar JR, Maritan A. Common attributes of native state structures of proteins, disordered proteins and amyloid. Proc Natl Acad Sci USA 2006;103:6883–6888.
33. Borroguero JM, Urbanc B, Lazo ND, Buldyrev SV, Teplow DB, Stanley HE. Folding events in the 21–30 region of amyloid beta-protein studied in silico. Proc Natl Acad Sci USA 2005;102:6015–6020.
34. Favrin G, Irback A, Mohanty S. Oligomerization of amyloid Abeta 16–22 peptides using hydrogen bonds and hydrophobicity forces. Biophys J 2004;87:3657–3664.
35. Fawzi NL, Chubukov V, Clark LA, Brown S, Heat-Gordon T. Influence of denatured and intermediate states of folding on protein aggregation. Protein Sci 2005;14:993–1003.
36. Nguyen HD, Hall CK. Spontaneous fibril formation by polyalanines discontinuous molecular dynamics simulations. J Am Chem Soc 2006;128:1890–1901.
37. Urbanc B, Cruz L, Ding F, Sammond D, Khare S, Buldyrev SV, Stanley HE, Dokholyan NV. Molecular dynamics simulation of amyloid beta dimer formation. Biophys J 2004;87:2310–2321.
38. Wei G, Mousseau N, Derreumaux P. Sampling the self-assembly pathways of KFFE hexamers. Biophys J 2004;87:3648–3656.
39. Lam AR, Teplow DB, Stanley HE, Urbanc B. Effects of the artic ($e^{22} \rightarrow g$) mutation on amyloid β-protein folding: discrete molecular dynamics study. J Am Chem Soc 2008;130:17413–17422.
40. Rojas A, Liwo A, Browne D, Scheraga HA. Mechanism of fiber assembly: treatment of Aβ peptide aggregation with a coarse-grained united residue force field. J Mol Biol 2010;404:537–552.
41. Urbanc B, Betnel M, Cruz L, Bitan G, Teplow DB. Elucidation of amyloid β protein oligomerization mechanisms: discrete molecular dynamics study. J Am Chem Soc 2010;132:4266–4280.
42. Go N, Scheraga HA. On the use of classical statistical mechanics in the treatment of polymer chain conformations. Macromolecules 1976;9:535–542.
43. Alm E, Baker D. Matching theory and experiment in protein folding. Curr Opin Struct Biol 1999;9:189–196.
44. Baker D. A surprising simplicity to protein folding. Nature 2000;405:39–42.
45. Clementi C, Nymeier H, Onhucic J. Topological and energetic factors: what determines the structural details of the transition state ensemble and en-route intermediates for protein folding? An investigation for small globular proteins. J Mol Biol 2000;298:937–953.
46. Hubner IA, Oliveberg M, Shakhnovich EI. Simulation, experiment and evolution: understanding nucleation in protein S6 folding. Proc Natl Acad Sci USA 2004;101:8354–8359.
47. Lam AR, Borreguero JM, Ding F, Dokholyan NV, Buldyrev SV, Stanley HE, Shaknovich E. Parallel folding pathways in the SH3 domain protein. J Mol Biol 2007;373:1348–1380.
48. Levy Y, Cho SS, Onuchic JN, Wolynes PG. A survey of flexible protein binding mechanisms and their transition states using native state topology based energy landscape. J Mol Biol 2005;346:1121–1145.
49. Micheletti C, Banavar JR, Maritan A, Seno F. Protein structures and optimal folding from a geometrical variational principle. Phys Rev Lett 1999;82:3372–3375.
50. Sulkowska JI, Sulkowski P, Onuchic J. Dodging the crisis of folding proteins with knots. Proc Natl Acad Sci USA 2009;106:3119–3124.
51. Ding F, Dokholyan NV, Buldyrev SV, Stanley HE, Shaknovich EI. Molecular dynamic simulation of the SH3 domain aggregation suggests a generic amyloidogenesis mechanism. J Biol Mol 2002; 324:851–857.
52. Jang H, Hall CK, Zhou Y. Assembly and kinetic folding pathways of a tetrameric β-sheet complex: molecular dynamics simulations on simplified off-lattice protein models. Biophys J 2004;86:31–49.
53. Bryngelson JD, Wolynes PG. Spin glasses and the statistical mechanics of protein folding. Proc Natl Acad Sci USA 1987;84:7524–7528.
54. Greenwald J, Buthz C, Ritter C, Kwiatkowski W, Choe S, Maddelein ML, Ness F, Cescau S, Soragni A, Leitz D, Saupe SJ, Riek R. The mechanisms of prion inhibition by HET-s. Mol Cell 2010;38:889–899.
55. Blackley HKL, Sanders GHW, Davies MC, Roberts CJ, Tendler SJB, Wilkinson MJ. In-situ atomic force microscopy study of beta-amyloid fibrillization. J Mol Biol 2000;298:833–840.
56. DePace AH, Weissman JS. Origins and kinetic consequences of diversity in sup35 yeast prion fibers. Nat Struct Biol 2002;9:389–396.
57. Fawzi NL, Okabe Y, Yap E-H, Head-Gordon T. Determining the critical nucleus and mechanism of fibril elongation of the Alzheimer's abeta1–40 peptide. J Mol Biol 2007;365:535–550.
58. Hoang TX, Trovato A, Seno F, Banavar JR, Maritan A. Geometry and symmetry presculpt the free-energy landscape of proteins. Proc Natl Acad Sci USA 2004;101:7960–7964.
59. Tesi MC, vanRensburg EJJ, Orlandini E, Whittington SG. Monte Carlo study of the interacting self-avoiding walk model in three dimensions. J Stat Phys 1996;82:155–181.
60. Metropolis N, Rosenbluth AW, Rosenbluth MN, Teller AH, Teller E. Equations of state calculations by fast computing machines. J Chem Phys 1953;21:87–92.
61. Wang FG, Landau DP. Efficient, multiple-range random walk algorithm to calculate the density of states. Phys Rev Lett 2001;86:2050–2053.
62. Kusumoto Y, Lomakin A, Teplow DB, Benedek GB. Temperature dependence of amyloid β-protein fibrillation. Proc Natl Acad Sci USA 1998;95:12277–12282.
63. Petkova AT, Ishii Y, Balbach JJ, Antzutkin ON, Gordon DJ, Meredith SC, Tycko R. A structural model for Alzheimer's beta-amyloid fibrils based on experimental constraints from solid state NMR. Proc Natl Acad Sci USA 2002;99:16742–16747.

64. Petkova AT, Yau W-M, Tycko R. Experimental constraints on quaternary structure in Alzheimer's beta-amyloid fibrils. Biochemistry 2006;45:498–512.
65. Krishnan R, Lindquist SL. Structural insights into a yeast prion illuminate nucleation and strain diversity. Nature 2005;447:453–457.
66. Shewmaker F, Wickner RB, Tycko R. Amyloid of the prion domain of Sup35p has an in-register parallel beta-sheet structure. Proc Natl Acad Sci USA 2006;103:19754–19759.
67. Tessier PM, Lindquist SL. Unraveling infectious structures, strain variants and species barriers for the yeast prion [PSI+]. Nat Struct Mol Biol 2009;16:598–605.
68. Trovato A, Chiti F, Maritan A, Seno F. Insight into the structure of amyloid fibrils from the analysis of globular proteins. PLoS Comput Biol 2006;2:1608–1618.
69. Trovato A, Seno F, Tosatto SCE. The PASTA server for protein aggregation prediction. Protein Eng Des Sel 2007;20:521–523.
70. Miyazawa S, Jernigan RL. Residue–residue potentials with a favorable contact pair term and an unfavorable high packing density term, for simulation and threading. J Mol Biol 1996;256:623–644.
71. Fang Q, Shortle D. A consistent set of statistical potentials for quantifying local side-chain and backbone interactions. Proteins 2005;60:90–96.
72. Wasmer C, Shutz A, Loquet A, Buhtz C, Greenwald J, Riek R, Bockmann A, Meier BH. The molecular organization of the fungal prion HET-s in its amyloid form. J Mol Biol 2009;319:1523–1526.
73. Zamparo M, Trovato A, Maritan A. Simplified exactly solvable models for beta-amyloid aggregation. Phys Rev Lett 2010;105:108102.